Gravity Wave Activity in the Atmosphere of Mars During the 2018 Global Dust Storm: Simulations With a High-Resolution Model

Takeshi Kuroda[1], Alexander S. Medvedev[2], and Erdal Yiğit[3]

[1]Department of Geophysics, Tohoku University, Sendai, Japan.
[2]Max Planck Institute for Solar System Research, Göttingen, Germany.
[3]Department of Physics and Astronomy, George Mason University, Fairfax, Virginia, USA.

Key Points:

- Gravity wave activity during the dust storm reduces by a factor of two or more in the troposphere
- The reduction is caused by convective and baroclinic stabilization of the atmosphere
- Wave energy and fluxes increase in the middle atmosphere due to favorable propagation conditions

Corresponding author: Takeshi Kuroda, tkuroda@tohoku.ac.jp

Abstract

Gravity wave activity in the lower and middle atmosphere of Mars during the global dust storm of 2018 has been studied for the first time using a high-resolution (gravity wave-resolving) general circulation model. Dust storm simulations were compared with those utilizing the climatological distribution of dust in the absence of storms. Both scenarios are based on observations of the dust optical depth by the Mars Climate Sounder instrument on board the Mars Reconnaissance Orbiter. The modeling reveals a reduction of the wave activity by a factor of two or more in the lower atmosphere, which qualitatively agrees with recent observations. It is associated with a decline of gravity wave generation due to baroclinic and convective stabilization of the Martian troposphere induced by the increased amount of airborne aerosols during the storm. Contrary to the decrease of GW activity in the lower atmosphere, wave energy and momentum fluxes in the middle atmosphere increase by approximately the same factor. This enhancement of gravity wave activity is caused by the changes in the large-scale circulation, most importantly in the mean zonal wind, which facilitate vertical wave propagation by allowing for a greater portion of gravity wave harmonics originated in the lower atmosphere to avoid filtering on their way to upper layers.

Plain Language Summary

Gravity waves (GWs) are oscillations of wind, temperature, pressure and density that originate in the dense lower atmosphere. They grow in amplitude upon propagation upward, and represent a major driving force in the thinner middle and upper atmosphere. GWs are difficult to account for in general circulation models (GCMs), because their scales are smaller than the resolution of the majority of such models. To circumvent this, we employ a high-resolution model that can explicitly resolve a significant portion of the GW spectrum. We showed that global planet-encircling dust storms as observeed in 2018 significantly alter the circulation of the Martian atmosphere and reduce GW generations in the lower atmosphere, due to the increased stability of the tropospheric flow with respect to disturbances of small and large scales. The surprising effect transpired in the simulations is the enhancement of GW activity in the middle atmosphere, which happens despite the weaker sources in the lower atmosphere. We explain it by changes in the large-scale circulation that facilitate upward propagation of waves originated below. Our simulations predict even greater dust storm-induced jump

in gravity wave activity in the thermosphere, which could be of great importance for the safety of Mars orbiters.

1 Introduction

Gravity waves (GWs) exist in atmospheres of all planets with convectively stable stratification. They transport energy and momentum from denser tropospheres to thinner upper levels (Yiğit & Medvedev, 2019). Effects produced by GWs are particularly strong in the middle and upper atmospheres of Earth and Mars (see recent reviews of Yiğit & Medvedev, 2015; Medvedev & Yiğit, 2019, correspondingly), thus making them a major dynamical mechanism that couples the lower and upper atmospheres on both planets. Being relatively small in size (from tens to hundreds of kilometers horizontal wavelength) and short-lived (periods from a few minutes to several hours), GWs are thought to strongly affect the Martian global circulation. They close and even reverse zonal jets in the middle atmosphere (Barnes, 1990; Medvedev et al., 2011a; Gilli et al., 2020), enhance the meridional circulation, the upwelling part of which amplifies the transport of water into the thermosphere (Shaposhnikov et al., 2019) and the descending branch leads to the thermospheric polar warmings (Bougher et al., 2006; Medvedev et al., 2011b). GW-induced downward transport of heat is the second-largest cooling mechanism in the thermosphere (after molecular heat conduction) that explains the observed meridional temperature structure on Mars (Medvedev & Yiğit, 2012) and Earth (Yiğit & Medvedev, 2009). Local fluctuations of temperature associated with GWs facilitate formation of mesospheric CO_2 clouds (Spiga et al., 2012; Yiğit et al., 2015, 2018), while GW-induced density disturbances significantly impact spacecraft performing aerobraking operations in the lower thermosphere (Jesch et al., 2019; Vals et al., 2019).

A detailed knowledge of GW activity is required for quantifying the wave influence on the dynamics and energetics of planetary atmospheres. Most of information on spectral and spatio-temporal characteristics of GWs in the lower atmosphere of Mars has been collected using remote sensing from orbiters. These techniques include radio occultations and infrared sounding (e.g., Creasey et al., 2006; Altieri et al., 2012; Ando et al., 2012; Wright, 2012). Recently, Heavens et al. (2020) provided a multi-annual climatology of global GW activity based on retrievals from the Mars Climate Sounder (MCS) instrument on board Mars Reconnaissance Orbiter (MRO). In particular, it covered the period of the global dust storm (GDS) that occurred in 2018 during the Martian year 34

(MY34). Such planet encircling storms do occasionally happen in the second half of the year, either at equinoxes, or around northern winter solstices as observed in 2007 during MY28 (e.g., Montabone et al., 2015). They dramatically impact the state and global circulation of the atmosphere (see, e.g., the review of Medvedev et al., 2011c). To date, little is known about the influence of dust storms on GW generation, propagation and associated effects in the middle and upper atmosphere. On one hand, the only (to the best of our knowledge) dedicated modeling study indicated an increased level of GW activity in the middle atmosphere of the northern winter hemisphere during the solstitial GDS (Kuroda et al., 2009). On the other hand, Heavens et al. (2020) recently reported on a significant reduction of wave activity in the lower atmosphere during the MY34 GDS. In this paper, we address this gap in knowledge of GW processes by performing for the first time simulations for the MY34 dust conditions using a high-resolution Martian general circulation model (MGCM).

Atmospheric models with conventional resolution do not capture GWs and have to parameterize the effects of subgrid-scale GWs instead (Yiğit & Medvedev, 2017; Medvedev & Yiğit, 2019). These parameterizations require constraints from observations that are not readily available and, most importantly, a specification of wave sources in the lower atmosphere. High-resolution models are computationally expensive, however they do self-consistently simulate, at least, a part of GW spectrum and processes of wave generation, propagation and obliteration. Thus, they may provide a realistic proxy for not yet available observations. The GW-resolving model used in this study is the high-resolution version of the extensively tested and validated MGCM (Kuroda et al., 2005). It provided a first global view of the GW field in the Martian lower and middle atmosphere (Kuroda et al., 2015), detailed spectral characteristics and field parameters during equinoxes and solstices (Kuroda et al., 2016), and the annual climatology of GW activity for a typical Martian year without dust storms (Kuroda et al., 2019). In this paper, we apply the observed distributions of dust during MY34 to infer the GDS-induced changes in GW activity and analyze their physical causation.

In the text to follow, the model and simulation setup are described in section 2. The obtained background circulation, GW activity in the lower and middle atmosphere are discussed in section 3. Conclusions are given in section 4.

2 Model Description and Experiment setup

The simulations presented in this study have been performed with a high-resolution version of the MGCM based on the hydrostatic dynamical spectral core of the terrestrial Model for Interdisciplinary Research On Climate (MIROC) developed in collaboration by the Atmosphere and Ocean Research Institute (AORI), the University of Tokyo, the National Institute of Environmental Studies (NIES), and the Japan Agency for Marine-Earth Science and Technology (JAMSTEC) (Hasumi & Emori, 2004; Sakamoto et al., 2012). The Martian GCM called DRAMATIC (Dynamics, RAdiation, MAterial Transport and their mutual InteraCtions) includes the package of physical parameterizations described in full detail in the papers of Kuroda et al. (2005, 2013). This model with conventional resolution has been applied to studying various atmospheric and paleoclimate phenomena on Mars (e.g., Kuroda et al., 2007, 2009; Kamada et al., 2020). For current simulations, the model was run at the T106 spectral truncation. This corresponds to $\sim 1.1^\circ \times 1.1^\circ$, or $\sim 67 \times 67$ km horizontal resolution. GCMs with compatible resolution ($\sim$T213) have been applied for studying GWs in the atmosphere of Earth (e.g., Sato et al., 2012). This setup does not capture smaller horizontal-scale convectively generated harmonics, however it resolves waves excited by flow over topography and unstable weather phenomena. The vertical domain extends from the surface to the middle atmosphere ($\sim$80-100 km) and is represented by 49 sigma-levels, as described in Kuroda et al. (2016, Table 1).

Heating and cooling due to radiative transfer in airborne aerosols is the major forcing mechanism that drives the circulation in the lower and middle atmosphere of Mars. At present, no MGCM can self-consistently reproduce the dust storms observed on Mars: their spontaneous onset, growth and decay. Therefore, in order to achieve most realistic simulations, we imposed dust distributions based on observations. For that, we used the total dust opacity derived by Montabone et al. (2020) over MY34 from the MCS measurements and assumed the vertical distribution of dust mixing ratio after (Conrath, 1975). Then, heating and cooling rates due to absorption and emission by atmospheric dust in solar and IR wavelengths (between 0.2 and 200 μm) were interactively computed and used for driving the circulation. The employed radiation scheme considers 24 representative wavelength bands: 12 in the visible and 12 in IR. The simulation with the "MY34 dust scenario" is compared with that using the "low-dust" scenario, which is based on multi-annual observations with dust storms removed (Kuroda et al., 2019).

3 Results

3.1 Background Circulation

The GDS of MY34 rapidly developed from a regional dust storm in the early northern fall around $L_s = 185°$ and 190°, i.e., in the late May - early June of 2018. In a few sols, the lifted dust rapidly encircled the planet, thus giving rise to the equinoctial GDS. The peak of the dust load lasted until approximately $L_s = 220°$, followed by the gradual decrease until $L_s \approx 290°$. Figure 1 shows the simulated background atmospheric characteristics at the midst of the storm: the zonal mean temperature and zonal wind averaged between $L_s = 195°$ and 220° (17 June and 29 July, 2018, correspondingly). Contour lines denote the values from the MY34 simulation, whereas the shades present the differences with the "low-dust" run. The temperature structure clearly demonstrates a typical response to the increased amount of airborne aerosol: cooling near the surface by 20-25 K due to the limited penetration of solar radiation and heating above by more than 30 K due to the intensified absorption by lifted aerosols. Such changes enhance both convective and baroclinic stability of the atmosphere. It is seen that the vertical temperature gradients decrease in the lower atmosphere, thus suppressing the development of convection and the associated GW sources. On the other hand, the enhanced convective stability (larger Brunt-Väisälä frequencies) facilitates vertical propagation of GW harmonics that were excited by other mechanisms. Figure 1a also demonstrates the decrease of the near-surface meridional temperature gradient in the middle and high latitudes of both hemispheres. This leads to stabilization of the mean zonal flow, which inhibits the development of baroclinic planetary waves (Kuroda et al., 2007), and potentially limits generation of large-scale inertia-gravity waves (Plougonven & Snyder, 2007).

Figure 1b illustrates the changes in the mean zonal wind produced by the GDS. Under the "low-dust" conditions, the equinoctial circulation consists of two westerly jets in both hemispheres and a weak (~ 10 m s^{-1}) equatorial easterly jet. The former two are maintained by the zonally directed Coriolis force associated with the two hemispheric meridional cells, while the latter is caused by excitation of thermal tides (Lewis & Read, 2003). During the dust storm, both westerly jets accelerated to more than 60 m s^{-1} in the southern hemisphere and $\sim$120 m s^{-1} in the northern one. The equatorial easterly jet moved higher following the elevation of the layer of most intense absorption of solar radiation and, consequently, of tide generation. Another remarkable feature is the

poleward shift of the westerly jets in the middle atmosphere of both hemispheres, which is evident from the differences plotted by shades. This is the result of the intensification of the meridional circulation, another manifestation of which is the warming in polar regions due to the diabatic heating by the downward parts of the hemispheric transport cells (Wilson, 1997; Hartogh et al., 2007; Medvedev & Hartogh, 2007). In the northern hemisphere during the dust storm, the westerly jet noticeably tilts with height from the equator to pole. This is accompanied by the decrease of the wind speed below and increase above, which substantially alters vertical propagation of GWs, as will be discussed in section 3.5. Overall, our simulations confirm the notion made in the paper of Medvedev et al. (2013) that dust storms modify the circulation pattern to what it is expected to be later in the season. Thus, the westerly jet in the northern fall hemisphere becomes as strong as it normally is during winters.

The timing of the MY34 GDS is very close to that of the event occurred in MY25. The latter was modeled with the different MAOAM (MPI) MGCM having a conventional (spectral truncation T21, or $\approx 5.6^\circ$) resolution, whose domain extended well into the thermosphere (Medvedev et al., 2013). Therefore, it is instructive to compare the two simulations. They are markedly similar in terms of the latitude-altitude structure and magnitudes. This includes the strength of the westerlies (also 60 and 120 m s^{-1} in the southern and northern hemispheres, respectively), the poleward tilt with height of the northern hemisphere jet and the deepened equatorial easterlies (Medvedev et al., 2013, Fig. 5d). The temperature distribution and its latitudinal structure along with magnitudes of the temperature changes are also very close (Medvedev et al., 2013, Fig. 4d). This indicates that the atmospheric response to major dust storms is likely robust and repeatable.

3.2 Spatial Distribution of Gravity Wave Activity in the Lower Atmosphere

Wave activity can be characterized by various quantities. Due to the fluctuating nature of the wave field, quadratic quantities are particularly useful, since they do not depend on phases. One of them is the potential energy (per unit mass) E_p

$$E_p = \frac{1}{2}\left(\frac{g}{N}\right)^2\left(\frac{T'}{\overline{T}}\right)^2, \tag{1}$$

where g denotes the acceleration of gravity, N is the Brunt-Väisälä frequency, $\bar{T}$ and T' are the mean and disturbed (wave) components of temperature T, respectively. The former is defined in the model as the sum of only larger-scale spherical harmonics with total spectral wavenumbers $s \leq 60$, as described in detail in our previous papers (e.g., Kuroda et al., 2015, Sect. 3). Since T is normally measurable, E_p can be used for comparison with observations. Figure 2a presents the latitude-longitude cross-section of the simulated E_p for the same as in Figure 1 period ($L_s = 195° - 220°$) averaged between pressure levels p=100 and 10 Pa. The shading shows the difference in the E_p with respect to the low-dust case. The first thing immediately seen is the overall reduction of the GW activity in low- to middle latitudes of both hemispheres during the storm, with a maximum decrease of up to –9 J kg^{-1} around 120°W. A closer inspection of the changes plotted with shades and the values themselves (given by contours) reveals that E_p in these areas is approximately a half of that in the "low-dust" simulation. The spatial pattern of wave activity did not alter substantially. The maxima of E_p continue to be located in mountainous regions of Tharsis Montes, Alba Patera, Elysium and the northern part of Arabia Terra. The largest reduction of wave activity caused by the GDS takes place mainly in these areas as well. Globally, E_p is larger in mid- to high latitudes of the northern hemisphere. These regions coincide with the edges of the westerly jet, which are prone to baroclinic instability (Kuroda et al., 2007) and to generation of inertia-gravity waves by Kelvin and other planetary waves constituting the weather variability (Kuroda et al., 2016). The persistent enhancement of GW activity across all longitudes at these latitudes during the northern fall and winter was recently supported by observations using MCS–MRO data (Heavens et al., 2020).

For more direct comparison with the latter work, namely with the lower two rows of its Figures 27 and 28, we also plotted the quantity $\log_{10} \Omega_{GW} = (T'/\bar{T})^2$ in Figure 2b. Note that the averaging was performed over approximately the same as in the observations vertical interval. Qualitatively, the observations and simulations are strikingly similar. Both show the increased wave activity in the northern hemisphere with the maxima in the middle- to high latitudes. Both demonstrate a significant reduction of Ω_{GW} during the GDS of MY34, which is particularly strong in low latitudes of both hemispheres. Quantitatively, simulations produce larger values of Ω_{GW} and lesser reduction than those found by Heavens et al. (2020) in observations. Thus, the activity in terms of $\log_{10} \Omega_{GW}$ decreases over the equator to less than -6.5 ($T'/\bar{T} < 0.05\%$) in observations, whereas

in simulations these values drop to only ≈ -4.8 ($T'/\bar{T} \approx 0.4\%$). For the low dust conditions, these values are around -6 (0.1%) in observations and -4 (1%) in the simulation. In areas of large wave activity, the agreement is better: Ω_{GW} is between -4.5 and -5 ($T'/\bar{T}$ between 0.5% and 0.3%) in observations during the storm vs around -4 (1%) in the simulation. This points out to a possible reason for the quantitative disagreement: small temperature fluctuations are difficult to detect with the MCS instrument, and the analysis produced values close to zero, whereas such problem does not exist in simulations. Another possible reason is that MCS observes a somewhat different part of the GW spectrum than that simulated by the MGCM. Heavens et al. (2020) state that MCS senses predominantly harmonics with shorter horizontal (10-30 km) and longer vertical (10 to 50 km) wavelengths, while our model well resolves shorter vertical wavelengths and does not resolve horizontal ones smaller than $\sim 2\times67$ km. Despite these differences, the agreement in terms of reduction of the GW activity during the storm as well as its spatial distribution provides an optimism that both observations and modeling capture the GW physics well.

Another quadratic (with respect to fluctuating variables) characteristic of wave activity is the vertical flux of horizontal wave momentum per unit mass, or, briefly, momentum flux. Unlike the potential energy, it is a vector and non-positively defined quantity, which is expressed as $\mathbf{F} = (\overline{u'w'}, \overline{v'w'})$, where u', v' and w' are the disturbances with total spectral wavenumbers $s \geq 61$ of the horizontal, meridional and vertical wind, correspondingly, and bars denote an appropriate averaging. The momentum carried by a GW harmonic is directed along its horizontal phase velocity. Since a wave spectrum is composed of multiple harmonics traveling in different directions, the total momentum is the vector sum of all components. Thus, the momentum flux is not necessarily proportional to wave energy, because contributions of harmonics propagating in opposite direction cancel each other. The flux may change signs with height not due to addition (generation) of new harmonics, but because of selective filtering of waves, whose phase speed c approaches $\bar{u}$.

Momentum flux is a very important characteristic of wave activity, since it is directly used in GW parameterizations employed by global circulation models. In particular, GW fluxes have to be explicitly specified at a certain height in the lower atmosphere considered to be a source level. Therefore, we plotted the simulated zonal and meridional components of $\mathbf{F}$ at 260 Pa pressure level in Figure 2 (panels c to f, color shades).

A significant reduction of the zonal momentum flux, both positive and negative, during the dust storm is clearly seen in Figures 2c and e. The decrease of the flux magnitude by a factor of 2 to 6 takes place almost throughout the planet. The remaining "hot spots" of GW activity are tied up to topographical features like the mountainous regions of Tharsis, Alba Patera, Elysium Mons and Arabia in the northern hemisphere, and Solis and the north-western slope of Hellas. A spotty low-latitude band of positive fluxes not apparently connected to the surface irregularities also weakened during the storm and moved southward, following the shift of the mean easterly winds. It is seen that fluxes have, generally, signs opposite to the zonal wind plotted with contours, except over mountains. This is the result of preferential filtering of GW harmonics traveling in the same as wind directions. Figures 2d and f demonstrate that the meridional fluxes also weakened during the storm. The meridional winds (shown with contours) are the indicators of non-zonal disturbances associated with planetary wave activity and other instabilities of the mean zonal flow. As seen in the figure, they are significantly reduced during the GDS. This leads to the conclusion that the decrease of GW fluxes is linked to weakening of wave generation by weather phenomena. Only orographycally-generated GWs persist during the dust storm. Recently it has been shown that the high-altitude winds can correlate with the underlying winds due to the influence of orographic GWs (Benna et al., 2019).

3.3 Temporal Evolution of Wave Activity in the Lower Atmosphere

We next consider time evolution of zonally averaged simulated quantities that characterize the GW field. To provide more insight, we plotted in contours the amplitudes of small-scale (with total spectral wavenumbers $s \geq 61$) temperature fluctuations $|T'|$ and wave kinetic energy per unit mass $E_k = (\overline{u'^2} + \overline{v'^2})/2$ along with their deviations from the "low-dust" run (color shades) as functions of the solar longitude L_s in Figures 3a and b, respectively. Both variables show an immediate drop after the onset of the MY34 GDS followed by gradual restoration to their previous values, as the amount of the lifted dust declined. A similar decrease has been reported in the work by Heavens et al. (2020, Figs. 22 and 23) based on the MCS data. The second drop at the end of the year coincides with the minor storm that started around $L_s = 320°$. The values again return back after the end of the event. The simulated amplitudes $|T'|$ are small, not to mention the changes, and are difficult to detect by remote sensing from the orbit. However, these are typical magnitudes of GWs in the troposphere, which then exponentially grow

upon their upward propagation. Kinetic energy is a quadratic quantity and, therefore, presents the change more clearly. Figure 3b shows that E_k is reduced approximately by a factor of two in the midst of the storm. Note also that the positions of maxima of temperature and wind fluctuations do not necessarily coincide. For example, GW-induced temperature fluctuations after the GDS ($L_s > 270°$) maximize in the midlatitudes of the northern hemisphere, whereas wind variations peak in low latitudes.

The evolution of the zonal component of the flux **F** and of the corresponding change with respect to the "low-dust" scenario are shown in Figures 3c and e with color shades, while the mean zonal wind $\bar{u}$ and the difference are superimposed with contours. The momentum fluxes are, generally, aligned with the wind. At the onset of the GDS, the weakening of the zonal jet in both hemispheres by ∼10 m s^{-1} is accompanied by the drop of $\overline{u'w'}$ by a factor of ewo and more. The equatorial easterlies also slowed down by ∼15 m s^{-1} (see contour lines in Figure 3e) and reversed at some places. The momentum flux followed on and dropped by up to 0.04 J kg^{-1}. The net result is the global reduction of GW momentum fluxes. Similar causality occurs for the meridional fluxes presented in Figures 3d and f. After the storm declines, the solstitial type of circulation establishes. The secondary dust storm that happened at the end of the northern winter also disrupted the cross-equatorial circulation, leading to to the decrease of GW momentum fluxes. Thus, both the major equinoctial and minor solstitial dust storms produced the same effect: they reduce GW activity in the troposphere. Remarkably, the circulation itself is again pushed by the minor storm toward the kind it is supposed to be later in the season, i.e., toward the equinoctial-type.

3.4 Gravity Wave Activity in the Middle Atmosphere

The behavior of the simulated GW activity in the middle atmosphere during the MY34 GDS differs from that in the lower atmosphere. Figures 4a and b show an increase of the amplitude of temperature fluctuations $|T'|$ by up to 2.5 K (∼10%) and kinetic energy E_k by a factor of ∼2 (more than 600 J kg^{-1}) at the 0.1 Pa pressure level. The increase takes place throughout the globe and maximizes in middle and high latitudes. The secondary dust storm at the end of the year is also accompanied by a similar increase, but of lesser magnitude. The westward GW momentum fluxes in the middle atmosphere are enhanced, in average also by about a factor of two following the weakening (and, in some places, reversal) of the westerly jets. At first sight, this contravenes the reduction

of fluxes in the lower atmosphere. Moreover, tropospheric $\overline{u'w'}$ are negative in the northern hemisphere and low latitudes of the southern one, while they are positive in the middle atmosphere, except in the northern high latitudes. This example indicates that the spectrum of GWs is broad and composed of harmonics traveling in opposite directions, thus carrying positive and negative momentum. The apparent contradiction resolves, if selective filtering by the mean wind in the course of vertical wave propagation is taken into account. A similar behavior of GWs occurs in Earth's atmosphere during sudden stratospheric warmings, when the background wind abruptly changes (Yiğit & Medvedev, 2012, 2016). Even more dramatic increase of magnitude in the middle atmosphere is seen for meridional momentum fluxes (Figures 4d and f). They are positive in the southern hemisphere, negative in the northern one, and are directed against the mean meridional wind as well. The final stage of the GDS coincides with a rapid transition from the equinoctial two- to one-cell solstitial global circulation, and the meridional GW fluxes adjust accordingly. Note also a similar response during the main and secondary dust storms at the end of the MY34.

3.5 Vertical Propagation of Gravity Waves

The increase of GW activity in the middle atmosphere during the GDS despite the reduction in the lower atmosphere requires further discussion. For that, we consider vertical propagation of waves at two characteristic latitudes. One is at 60°N, where the storm-induced reduction of GW kinetic energy E_k in the lower atmosphere was relatively weak (Figure 3b, but increase in the middle atmosphere was largest (Figure 4b. According to the conventional picture of wave propagation through a background flow, which was originally introduced by Holton (1983) and subsequently explored with a variety of GCMs, a broad incident spectrum of GWs composed of harmonics moving in opposite directions experiences selective filtering. Harmonics, whose horizontal phase speeds c coincide with the mean wind $\bar{u}$, are absorbed by the flow in the vicinity of their respective critical levels $|c-\bar{u}| = 0$. In fact, as the phase speed approaches the background mean wind, GW dissipation rapidly increases as well. Those harmonics that avoid the filtering contribute to the wave activity in the middle and upper atmosphere. The surviving spectrum of waves typically includes harmonics traveling against the mean wind ($c < 0$) as well as those propagating eastward, but moving slower than the mean wind at the source level. Within

a strong westerly jet, $\bar{u} > 0$ varies a lot with height, which leads to obliteration of harmonics with a broad range of eastward phase speeds, i.e., $c > 0$.

Figure 5a shows the mean zonal wind $\bar{u}$ (contours) at 60°N for the MY34 simulation along with the difference with the "low-dust" run (color shades). It is seen that the wind gradually decreased by up to 25 m s^{-1} below ∼0.1 Pa and increased by up to 10 m s^{-1} above. This has enabled for more eastward harmonics moving faster than the local wind to penetrate above the 0.1 Pa pressure level. They delivered an additional E_k above this height, as is seen in Figure 5b (color shades). Note that this enhancement is even more significant near the top of the model due to the exponential vertical growths of kinetic wave energy per unit mass. Towards the end of the GDS (around $L_s = 240°$), the core of the jet moved lower (below the pressure level 0.5 Pa) and amplified. It halted vertical propagation of fast GW harmonics, and E_k above declined.

Another representative latitude to be considered is 15°N. It is where the drop of wave activity in the lower atmosphere was largest (Figure 3b), while the increase in the middle atmosphere was moderate (Figure 4b). Interactions of GW spectra with the mean flow in low latitudes differ from those in middle and high latitudes, because zonal winds are much weaker there compared to the core of the jet at middle latitudes. These winds, therefore, are able to absorb only wave harmonics with relatively slow horizontal phase speeds, while affecting the faster waves only to a minor degree. They, nevertheless, contain a great portion of the total wave energy of the GW spectrum, because the power density of the latter, generally, decreases with c in the lower atmosphere.

Figure 6 shows the evolution of the mean zonal wind and GW kinetic energy E_k at 15°N from the "low-dust" and MY34 simulations. It is seen that a sudden and strongest reduction of E_k in the lower atmosphere occurred at the onset of the GDS, lasted up to $L_s \sim 210°$, and then gradually declined (Figure 6b, color shades). The increase of activity in the middle atmosphere closely followed this pattern, with a small delay associated with the time required for GWs to reach upper levels. This process coincides with a rapid transformation of the mean circulation (contour lines). Without the dust storm (Figure 6), directions of the zonal wind alternate with height reflecting the semiannual oscillation in low latitudes (Kuroda et al., 2008; Ruan et al., 2019). They prevent (filter out) GW harmonics with phase velocities of up to $\sim \pm 20$ m s^{-1} (at $L_s \sim 210°$) from reaching the top. During the dust storm, the mean wind pattern has dramatically

changed. At first (before $L_s \sim 200°$), the westward wind disappeared, thus letting harmonics with negative c to penetrate the upper levels. After that, the westerly jet (centered around $p \sim 0.5$ Pa declined and was replaced by easterlies reaching to the very top of the model domain. This gave way up to slow GW harmonics with positive phase velocities.

The presented schematic consideration allows for interpreting the mechanism of GW activity increase in the upper Martian mesosphere during the MY34 GDS without invoking additional sources. It is based on the only assumption of broad GW spectra and is consistent with the conventional mechanism of wave-mean flow interactions. One of the consequences of this mechanism, which is yet to be explored using observations, would be even stronger increase of GW activity in the thermosphere.

4 Summary and Conclusions

For the first time, we investigated the behavior of the gravity wave (GW) activity in the Martian atmosphere during global dust storms (GDS) by performing high-resolution simulations with a GW-resolving Martian general circulation model (MGCM). For that, we imposed distributions of atmospheric aerosol based on observations from the Mars Climate Sounder instrument during Martian Year 34 (MY34), when a major GDS occurred in the early northern winter. The simulations have been compared with that for a dustless year based on multi-annual observations with periods of dust storms removed. The main inferences of this study can be summarized as follows.

1. GW activity during the MY34 GDS drops in the lower atmosphere (up to ∼40 km): kinetic and potential energy, vertical fluxes of horizontal momentum decrease by a factor of approximately two in the zonally average sense. Locally, GW activity reduces by a factor of up to six. Qualitatively, these results concur with the recent observational findings of Heavens et al. (2020). Quantitatively, simulations show less reduction, which can be partially explained by the model resolving somewhat different part of the GW spectrum: longer horizontal and shorter vertical scales.
2. The reduction is clearly linked to the decreased planetary wave activity due to the baroclinic stabilization of the lower atmosphere caused by the changed pattern of solar radiation absorption by airborne dust. The planetary wave activity and as-

sociated instabilities of atmospheric flow are a major mechanism of GW generation. The GDS produces also more stable lapse rates, which prevent the development of convective instability. The convectively generated GWs, whose horizontal scales are compatible with those of convective cells, are, however, not resolved by the model. Orographically-generated GWs are, apparently, less affected by the dust storm.

3. Despite the reduction of wave sources in the lower atmosphere, GW activity in the middle atmosphere approximately doubles. This increase is consistent with the conventional mechanism of wave-mean flow interactions: changes in the background zonal winds facilitate vertical propagation of GW harmonics by allowing a greater part of the incident spectrum to penetrate upper levels.
4. The response of the GW activity to the weaker regional dust storm, which occurred at the end of MY34, is similar to that during the GDS, although of smaller magnitude. Thus, the underlying mechanisms of inhibition of wave generation and of enhanced upward GW propagation during both storms are likely the same.

The reduction of GW sources during dust storms has to be accounted for in MGCMs with conventional (low) resolution employing GW parameterizations, if we are to improve representation of the dynamics of the middle and upper Martian atmosphere.

Acknowledgments

The modeling data supporting the figures presented in this paper are available at 10.5281/zenodo.3760271 and 10.5281/zenodo.3762945. TK was funded by the Japan Society for the Promotion of Science (JSPS) KAKENHI Grant Number JP19H00707, and also supported by Grant Numbers JP16K05552 and JP19K03980. The model runs were performed using the Fujitsu PRIMERGY CX600M1/CX1640M1 (Oakforest-PACS) at the Information Technology Center, The University of Tokyo.

References

Altieri, F., Spiga, A., Zasova, L., Bellucci, G., & Bibring, J.-P. (2012). Gravity waves mapped by the OMEGA/MEX instrument through O_2 dayglow at 1.27 μm: Data analysis and atmospheric modeling. *Journal of Geophysical Research: Planets*, *117*(E11). Retrieved from `https://agupubs.onlinelibrary`

.wiley.com/doi/abs/10.1029/2012JE004065 doi: 10.1029/2012JE004065

Ando, H., Imamura, T., & Tsuda, T. (2012). Vertical wavenumber spectra of gravity waves in the Martian atmosphere obtained from Mars Global Surveyor radio occultation data. *Journal of the Atmospheric Sciences*, *69*, 2906–2912. doi: 10.1175/JAS-D-11-0339.1

Barnes, J. R. (1990). Possible effects of breaking gravity waves on the circulation of the middle atmosphere of Mars. *Journal of Geophysical Research*, *95*, 1401–1421.

Benna, M., Bougher, S. W., Lee, Y., Roeten, K. J., Yiğit, E., Mahaffy, P. R., & Jakosky, B. M. (2019). Global circulation of mars' upper atmosphere. *Science*, *366*(6471), 1363–1366. Retrieved from https://science.sciencemag.org/content/366/6471/1363 doi: 10.1126/science.aax1553

Bougher, S. W., Bell, J. M., Murphy, J. R., López-Valverde, M. A., & Withers, P. G. (2006). Polar warming in the Mars thermosphere: Seasonal variations owing to changing insolation and dust distributions. *Geophysical Research Letters*, *33*. doi: 10.1029/2005GL024059

Conrath, B. J. (1975). Thermal structure of the Martian atmosphere during the dissipation of the dust storm of 1971. *Icarus*, *24*(1), 36–46. Retrieved from http://www.sciencedirect.com/science/article/pii/0019103575901566 doi: https://doi.org/10.1016/0019-1035(75)90156-6

Creasey, J. E., Forbes, J. M., & Hinson, D. P. (2006). Global and seasonal distribution of gravity wave activity in Mars' lower atmosphere derived from MGS radio occultation data. *Geophysical Research Letters*, *33*. doi: 10.1029/2005GL024037

Gilli, G., Forget, F., Spiga, A., Navarro, T., Millour, E., Montabone, L., ... Schofield, J. T. (2020). Impact of gravity waves on the middle atmosphere of Mars: A non-orographic gravity wave parameterization based on global climate modeling and MCS observations. *Journal of Geophysical Research: Planets*, *125*(3), e2018JE005873. Retrieved from https://agupubs.onlinelibrary.wiley.com/doi/abs/10.1029/2018JE005873 doi: 10.1029/2018JE005873

Hartogh, P., Medvedev, A. S., & Jarchow, C. (2007). Middle atmosphere polar warmings on Mars: simulations and study on the validation with sub-

millimeter observations. *Planetary and Space Science*, *55*, 1103–1112.

Hasumi, H., & Emori, S. (2004). K-1 coupled GCM (MIROC) description. University of Tokyo K-1 Tech. Rep. 1..

Heavens, N. G., Kass, D. M., Kleinböhl, A., & Schofield, J. T. (2020). A multiannual record of gravity wave activity in Mars's lower atmosphere from on-planet observations by the Mars Climate Sounder. *Icarus*, *341*, 113630. Retrieved from http://www.sciencedirect.com/science/article/pii/S0019103519305755 doi: https://doi.org/10.1016/j.icarus.2020.113630

Holton, J. R. (1983). The influence of gravity wave breaking on the general circulation of the middle atmosphere. *Journal of the Atmospheric Sciences*, *40*, 2497–2507.

Jesch, D., Medvedev, A. S., Castellini, F., Yiğit, E., & Hartogh, P. (2019, Oct). Density fluctuations in the lower thermosphere of Mars retrieved from the ExoMars Trace Gas Orbiter (TGO) aerobraking. *Atmosphere*, *10*(10), 620. Retrieved from http://dx.doi.org/10.3390/atmos10100620 doi: 10.3390/atmos10100620

Kamada, A., Kuroda, T., Kasaba, Y., Terada, N., Nakagawa, H., & Toriumi, K. (2020). A coupled atmosphere-hydrosphere global climate model of early Mars: A "cool and wet" scenario for the formation of water channels. *Icarus*, *338*, 113567. Retrieved from http://www.sciencedirect.com/science/article/pii/S0019103518300927 doi: https://doi.org/10.1016/j.icarus.2019.113567

Kuroda, T., Hashimoto, N., Sakai, D., & Takahashi, M. (2005). Simulation of the Martian atmosphere using a CCSR/NIES AGCM. *Journal of the Meteorological Society of Japan*, *83*(1), 1–19. doi: 10.2151/jmsj.83.1

Kuroda, T., Medvedev, A. S., Hartogh, P., & Takahashi, M. (2007). Seasonal changes of the baroclinic wave activity in the northern hemisphere of Mars simulated with a GCM. *Geophysical Research Letters*, *34*(9). Retrieved from https://agupubs.onlinelibrary.wiley.com/doi/abs/10.1029/2006GL028816 doi: 10.1029/2006GL028816

Kuroda, T., Medvedev, A. S., Hartogh, P., & Takahashi, M. (2008). Semiannual oscillations in the atmosphere of Mars. *Geophysical Research Letters*, *35*(23). Retrieved from https://agupubs.onlinelibrary.wiley.com/doi/abs/10.1029/2008GL036061 doi: 10.1029/2008GL036061

Kuroda, T., Medvedev, A. S., Hartogh, P., & Takahashi, M. (2009). On forcing the winter polar warmings in the Martian middle atmosphere during dust storms. *Journal of the Meteorological Society of Japan*, *87*(5), 913–921. doi: 10.2151/jmsj.87.913

Kuroda, T., Medvedev, A. S., Kasaba, Y., & Hartogh, P. (2013). Carbon dioxide ice clouds, snowfalls, and baroclinic waves in the northern winter polar atmosphere of Mars. *Geophysical Research Letters*, *40*(8), 1484–1488. Retrieved from `https://agupubs.onlinelibrary.wiley.com/doi/abs/10.1002/grl.50326` doi: 10.1002/grl.50326

Kuroda, T., Medvedev, A. S., Yiğit, E., & Hartogh, P. (2016). Global distribution of gravity wave sources and fields in the Martian atmosphere during equinox and solstice inferred from a high-resolution general circulation model. *Journal of the Atmospheric Sciences*, *73*, 4895–4909. doi: 10.1175/JAS-D-16-0142.1

Kuroda, T., Medvedev, A. S., Yiğt, E., & Hartogh, P. (2015). A global view of gravity waves in the Martian atmosphere inferred from a high-resolution general circulation model. *Geophysical Research Letters*, *42*(21), 9213–9222. Retrieved from `https://agupubs.onlinelibrary.wiley.com/doi/abs/10.1002/2015GL066332` doi: 10.1002/2015GL066332

Kuroda, T., Yiğit, E., & Medvedev, A. S. (2019). Annual cycle of gravity wave activity derived from a high-resolution Martian general circulation model. *Journal of Geophysical Research: Planets*, *124*(6), 1618–1632. Retrieved from `https://agupubs.onlinelibrary.wiley.com/doi/abs/10.1029/2018JE005847` doi: 10.1029/2018JE005847

Lewis, S. R., & Read, P. L. (2003). Equatorial jets in the dusty martian atmosphere. *Journal of Geophysical Research: Planets*, *108*(E4). Retrieved from `https://agupubs.onlinelibrary.wiley.com/doi/abs/10.1029/2002JE001933` doi: 10.1029/2002JE001933

Medvedev, A. S., & Hartogh, P. (2007). Winter polar warmings and the meridional transport on Mars simulated with a general circulation model. *Icarus*, *186*, 97–110.

Medvedev, A. S., Kuroda, T., & Hartogh, P. (2011c). Influence of dust on the dynamics of the martian atmosphere above the first scale height. *Aeolian Research*, *3*(2), 145–156. Retrieved from `http://www.sciencedirect.com/`

science/article/pii/S1875963711000401 doi: https://doi.org/10.1016/j.aeolia.2011.05.001

Medvedev, A. S., & Yiğit, E. (2012). Thermal effects of internal gravity waves in the Martian upper atmosphere. *Geophysical Research Letters*, *39*. doi: 10.1029/2012GL050852

Medvedev, A. S., & Yiğit, E. (2019). Gravity waves in planetary atmospheres: Their effects and parameterization in global circulation models. *Atmosphere*, *10*(9). Retrieved from https://www.mdpi.com/2073-4433/10/9/531 doi: 10.3390/atmos10090531

Medvedev, A. S., Yiğit, E., & Hartogh, P. (2011a). Estimates of gravity wave drag on Mars: indication of a possible lower thermosphere wind reversal. *Icarus*, *211*, 909–912. doi: 10.1016/j.icarus.2010.10.013

Medvedev, A. S., Yiğit, E., Hartogh, P., & Becker, E. (2011b). Influence of gravity waves on the Martian atmosphere: General circulation modeling. *Journal of Geophysical Research: Planets*, *116*. Retrieved from https://agupubs.onlinelibrary.wiley.com/doi/abs/10.1029/2011JE003848 doi: 10.1029/2011JE003848

Medvedev, A. S., Yiğit, E., Kuroda, T., & Hartogh, P. (2013). General circulation modeling of the Martian upper atmosphere during global dust storms. *Journal of Geophysical Research: Planets*, *118*, 1–13. doi: 10.1002/jgre.20163,2013

Montabone, L., Forget, F., Millour, E., Wilson, R. J., Lewis, S. R., Cantor, B., ... Wolff, M. J. (2015). Eight-year climatology of dust optical depth on mars. , *251*, 65–95. doi: 10.1016/j.icarus.2014.12.034

Montabone, L., Spiga, A., Kass, D. M., Kleinböhl, A., Forget, F., & Millour, E. (2020). Martian year 34 column dust climatology from Mars Climate Sounder observations: Reconstructed maps and model simulations. *Journal of Geophysical Research: Planets*, e2019JE006111. Retrieved from https://agupubs.onlinelibrary.wiley.com/doi/abs/10.1029/2019JE006111 (e2019JE006111 2019JE006111) doi: 10.1029/2019JE006111

Plougonven, R., & Snyder, C. (2007). Inertia-gravity waves spontaneously generated by jets and fronts. Part I: Different baroclinic life cycles. *Journal of the Atmospheric Sciences*, *64*(7), 2502–2520. Retrieved from https://doi.org/10.1175/JAS3953.1 doi: 10.1175/JAS3953.1

590 Ruan, T., Lewis, N. T., Lewis, S. R., Montabone, L., & Read, P. L. (2019). Investi-
591 gating the semiannual oscillation on Mars using data assimilation. *Icarus*, *333*,
592 404–414. Retrieved from http://www.sciencedirect.com/science/article/
593 pii/S0019103518306055 doi: https://doi.org/10.1016/j.icarus.2019.06.012

594 Sakamoto, T. T., Komuro, Y., Nishimura, T., Ishii, M., Tatebe, H., Shiogama, H.,
595 ... Kimoto, M. (2012). MIROC4h – A new high-resolution atmosphere-ocean
596 coupled general circulation model. *Journal of the Meteorological Society of*
597 *Japan. Ser. II*, *90*(3), 325–359. doi: 10.2151/jmsj.2012-301

598 Sato, K., Tateno, S., Watanabe, S., & Kawatani, Y. (2012). Gravity wave char-
599 acteristics in the southern hemisphere revealed by a high-resolution middle-
600 atmosphere general circulation model. *Journal of the Atmospheric Sci-*
601 *ences*, *69*(4), 1378–1396. Retrieved from https://doi.org/10.1175/
602 JAS-D-11-0101.1 doi: 10.1175/JAS-D-11-0101.1

603 Shaposhnikov, D. S., Medvedev, A. S., Rodin, A. V., & Hartogh, P. (2019). Sea-
604 sonal water "pump" in the atmosphere of Mars: Vertical transport to the
605 thermosphere. *Geophysical Research Letters*, *46*(8), 4161–4169. Retrieved
606 from https://agupubs.onlinelibrary.wiley.com/doi/abs/10.1029/
607 2019GL082839 doi: 10.1029/2019GL082839

608 Spiga, A., González-Galindo, F., López-Valverde, M.-A., & Forget, F. (2012). Grav-
609 ity waves, cold pockets and CO_2 clouds in the martian mesosphere. *Geophysi-*
610 *cal Research Letters*, *39*. doi: 10.1029/2011GL050343

611 Vals, M., Spiga, A., Forget, F., Millour, E., Montabone, L., & Lott, F. (2019).
612 Study of gravity waves distribution and propagation in the thermo-
613 sphere of Mars based on MGS, ODY, MRO and MAVEN density mea-
614 surements. *Planetary and Space Science*, *178*, 104708. Retrieved from
615 http://www.sciencedirect.com/science/article/pii/S0032063319300042
616 doi: https://doi.org/10.1016/j.pss.2019.104708

617 Wilson, R. J. (1997). A general circulation model simulation of the Martian polar
618 warming. *Geophysical Research Letters*, *24*(2), 123–126.

619 Wright, C. J. (2012). A one-year seasonal analysis of martian gravity waves
620 using mcs data. *Icarus*, *219*(1), 274–282. Retrieved from http://
621 www.sciencedirect.com/science/article/pii/S0019103512000899 doi:
622 https://doi.org/10.1016/j.icarus.2012.03.004

Yiğit, E., & Medvedev, A. S. (2009). Heating and cooling of the thermosphere by internal gravity waves. *Geophysical Research Letters*, *36*. doi: 10.1029/2009GL038507

Yiğit, E., & Medvedev, A. S. (2012). Gravity waves in the thermosphere during a sudden stratospheric warming. *Geophysical Research Letters*, *39*. doi: 10.1029/2012GL053812

Yiğit, E., & Medvedev, A. S. (2015). Internal wave coupling processes in Earth's atmosphere. *Advances in Space Research*, *55*(5), 983–1003. doi: 10.1016/j.asr.2014.11.020

Yiğit, E., & Medvedev, A. S. (2016). Role of gravity waves in vertical coupling during sudden stratospheric warmings. *Geoscience Letters*, *3*(1), 1–13. doi: 10.1186/s40562-016-0056-1

Yiğit, E., & Medvedev, A. S. (2017). Influence of parameterized small-scale gravity waves on the migrating diurnal tide in earth's thermosphere. *Journal of Geophysical Research: Space Physics*, *122*, 4846–4864. doi: 10.1002/2017JA024089

Yiğit, E., & Medvedev, A. S. (2019). Obscure waves in planetary atmospheres. *Physics Today*, *6*, 40–46. doi: 10.1063/PT.3.4226

Yiğit, E., Medvedev, A. S., & Hartogh, P. (2015). Gravity waves and high-altitude CO_2 ice cloud formation in the martian atmosphere. *Geophysical Research Letters*, *42*, 4294–4300. doi: 10.1002/2015GL064275

Yiğit, E., Medvedev, A. S., & Hartogh, P. (2018). Influence of gravity waves on the climatology of high-altitude martian carbon dioxide ice clouds. *Annales Geophysicae*, *36*(6), 1631–1646. Retrieved from `https://www.ann-geophys.net/36/1631/2018/` doi: 10.5194/angeo-36-1631-2018

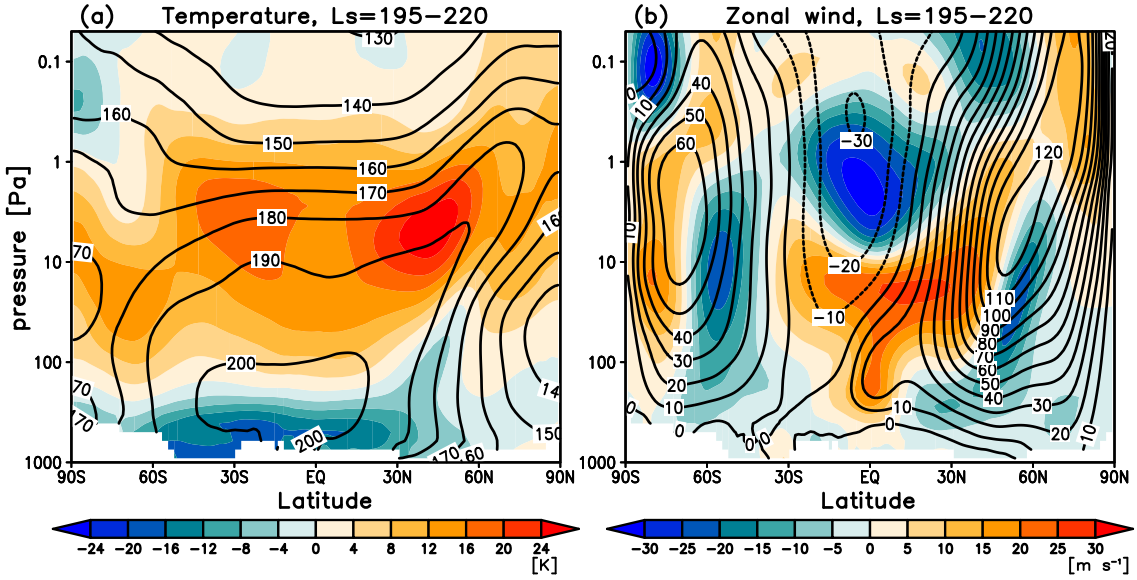

Figure 1. Latitude-altitude cross-sections of zonal-mean (a) temperature (K) and (b) zonal wind (m s^{-1}) averaged over L_s= 195°-220°. Contours denote the results for the MY34 dust scenario, shades show the difference with the "low-dust" simulation.

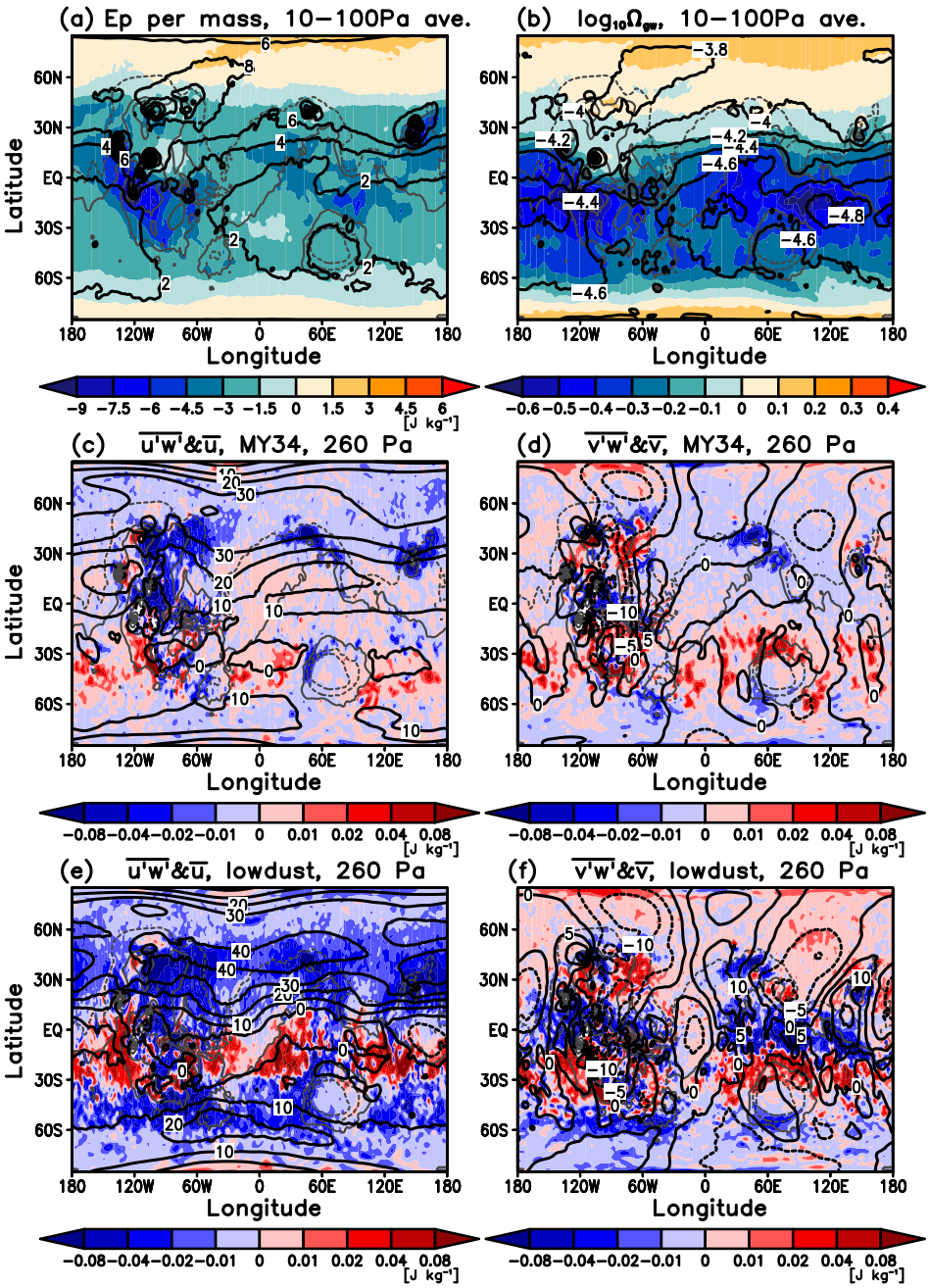

Figure 2. Longitude-latitude cross-sections of GW (a) potential energy per unit mass (J kg^{-1}) and (b) $\log_{10}\Omega_{GW}$ (Ω_{GW} =$\overline{T'^2}/\bar{T}^2$) averaged between 10–100 Pa and L_s= 195°-220°. In (a) and (b), the black contours present the results for the MY34 dust scenario, and shades denote the difference with the low-dust scenario. (c) shows the vertical flux of GW zonal momentum (per unit mass) $\overline{u'w'}$ (shades, in J kg^{-1}) and mean zonal wind $\bar{u}$ (black contours, in m s^{-1}) at the 260 Pa pressure level averaged between L_s= 195°-220° for the MY34 dust scenario. (d) is the same as (c) except for the vertical flux of meridional momentum (per unit mass) $\overline{v'w'}$ (shades) and mean meridional wind $\bar{v}$ (contours). (e) and (f) are the same as (c) and (d), respectively, except for the "low-dust" scenario. Grey contours present the Martian topography for all plots.

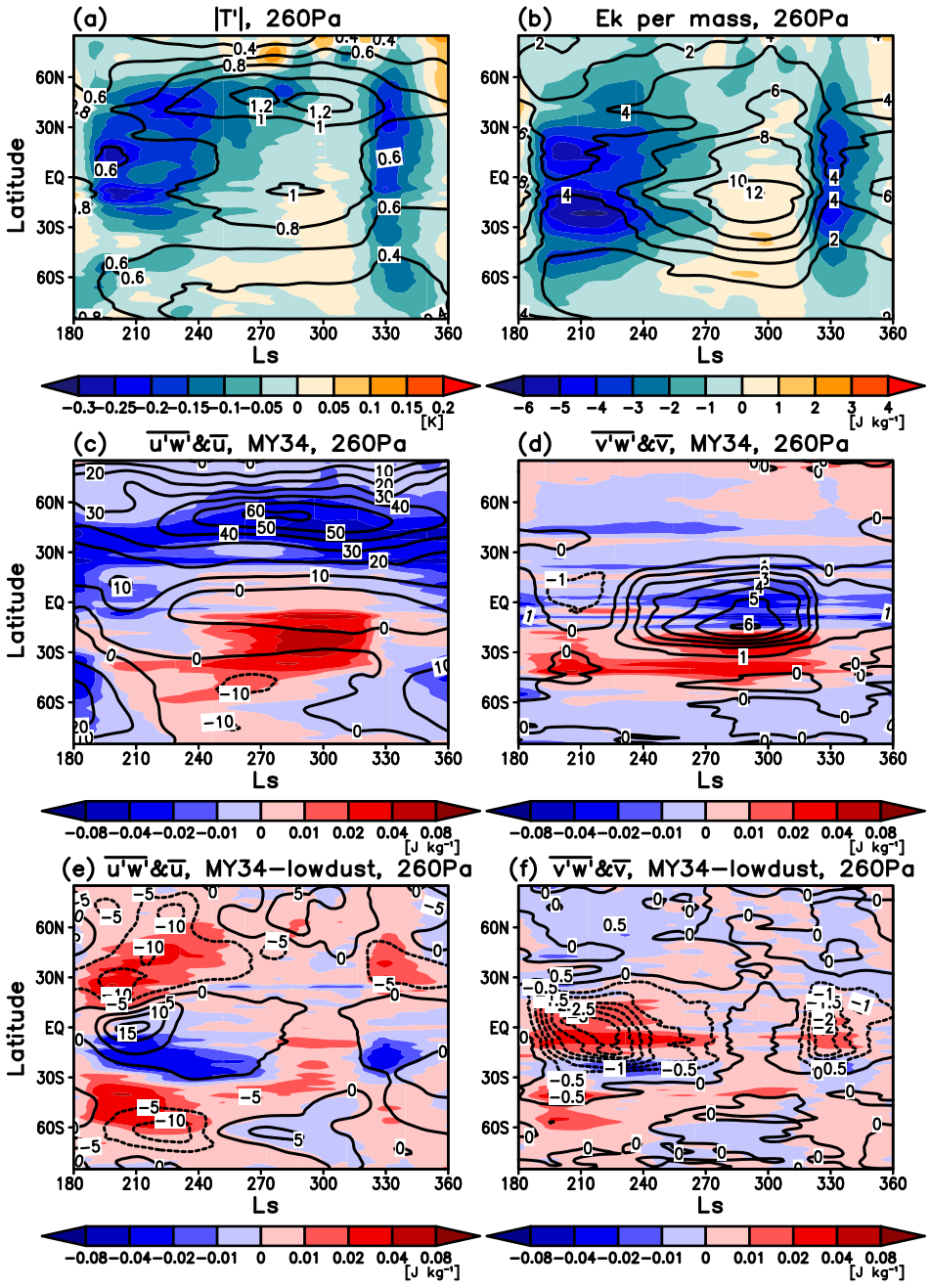

Figure 3. Seasonal-latitude distributions of the zonally averaged GW quantities in the troposphere (at the 260 Pa pressure level). (a) Amplitude of GW-induced temperature fluctuations $|T'|$ (K) and (b) GW kinetic energy E_k (J kg^{-1}). The black contours denote the results for the MY34 dust scenario, shades present the difference with respect to the "low-dust" simulation. (c) The vertical flux of GW zonal momentum (per unit mass) $\overline{u'w'}$ (shades, in J kg^{-1}) and the mean zonal wind $\bar{u}$ (black contours, in m s^{-1}) for the MY34 dust scenario. (d) is the same as (c) except for the vertical flux of meridional momentum (per unit mass) $\overline{v'w'}$ (shades) and the mean meridional wind $\bar{v}$ (black contours). (e) and (f) are the same as (c) and (d), respectively, except for the difference with the "low-dust" simulation.

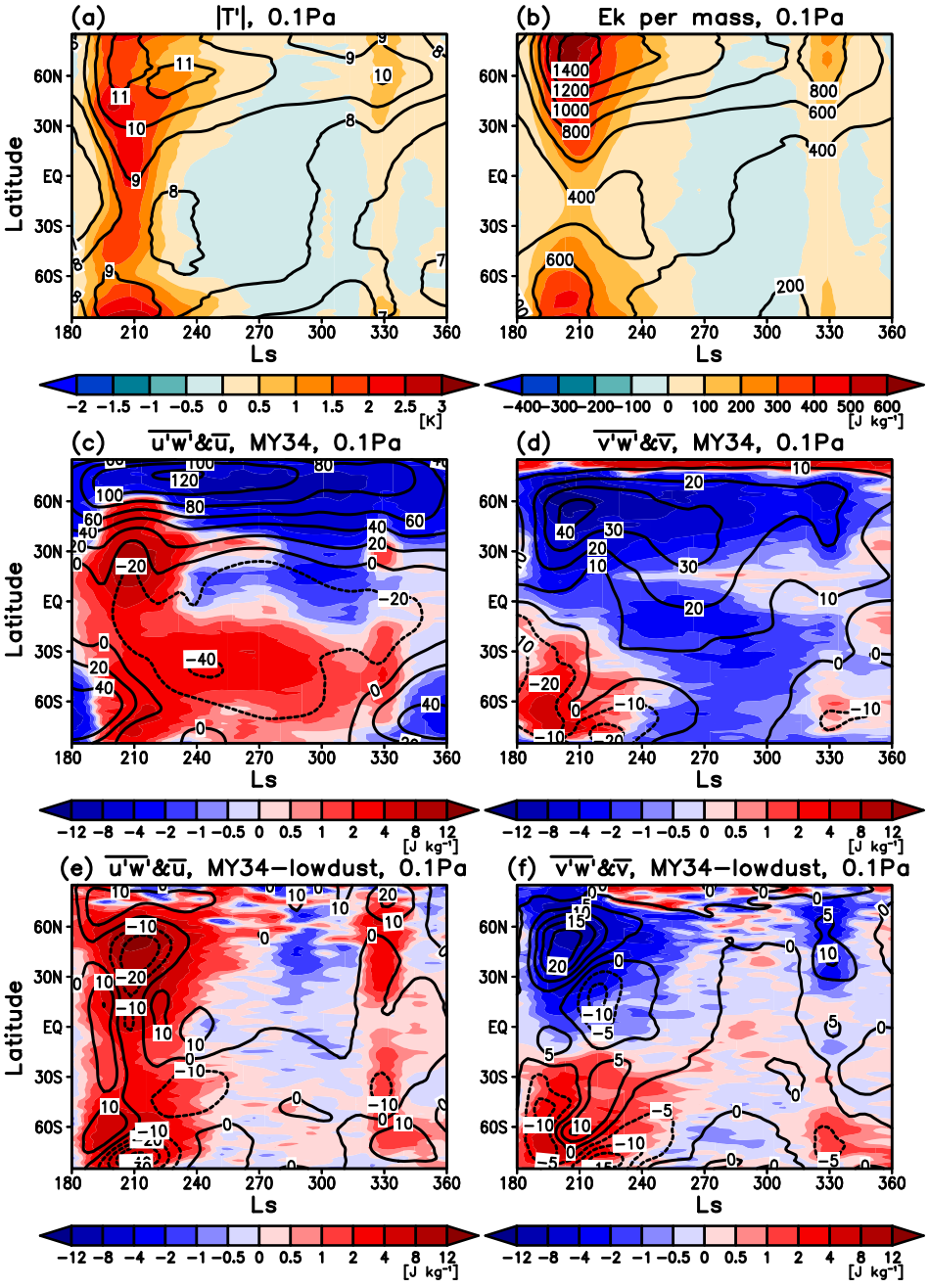

Figure 4. Same as in Figure 3, except in the mesosphere at the 0.1 Pa pressure level.

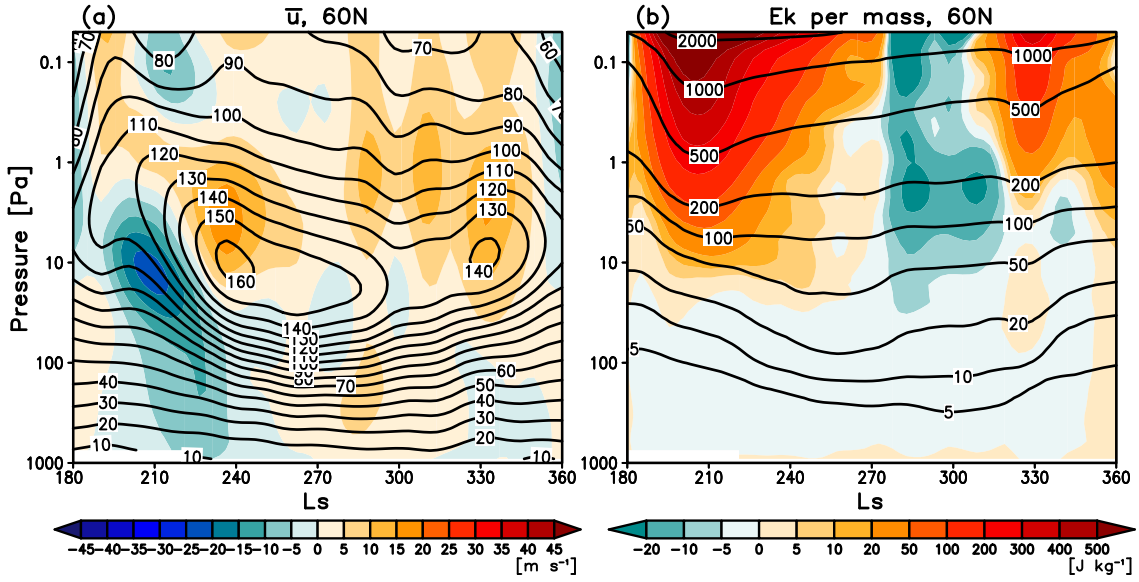

Figure 5. Seasonal-vertical distributions (contours) of a) the zonal mean wind $\bar{u}$ (m s^{-1}) and b) wave kinetic energy per unit mass E_k (J kg^{-1}). Color shades denote the difference of the corresponding quantities with the "low-dust" run.

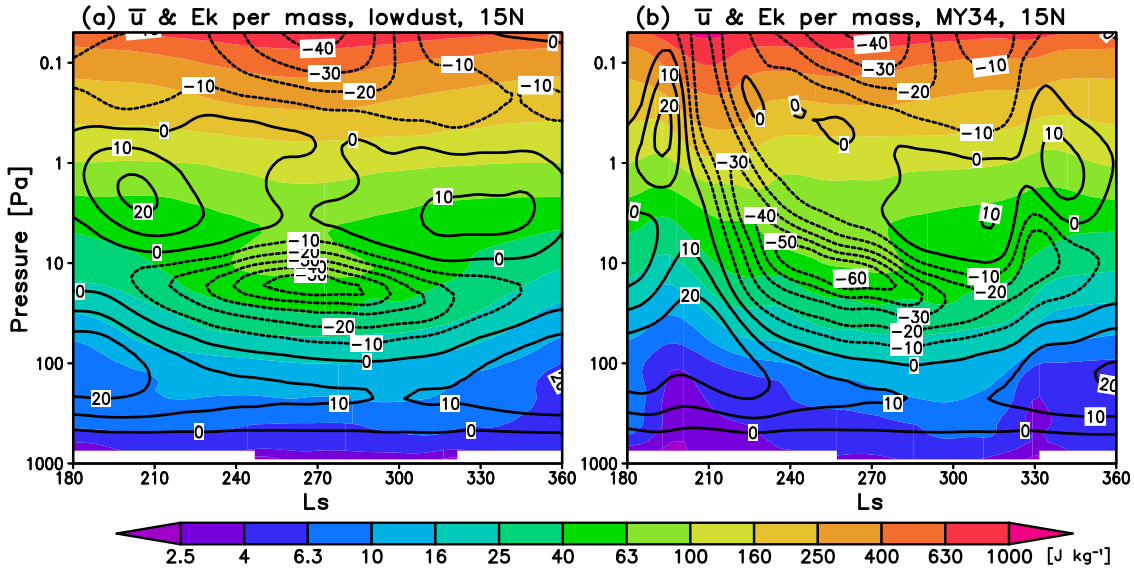

Figure 6. Seasonal-vertical distributions of the mean zonal wind (contours, in m s^{-1}) and wave kinetic energy E_k (color shades, in J kg^{-1}) at 15°N from the (a) "low-dust" and (b) MY34 runs.

Figure 1.

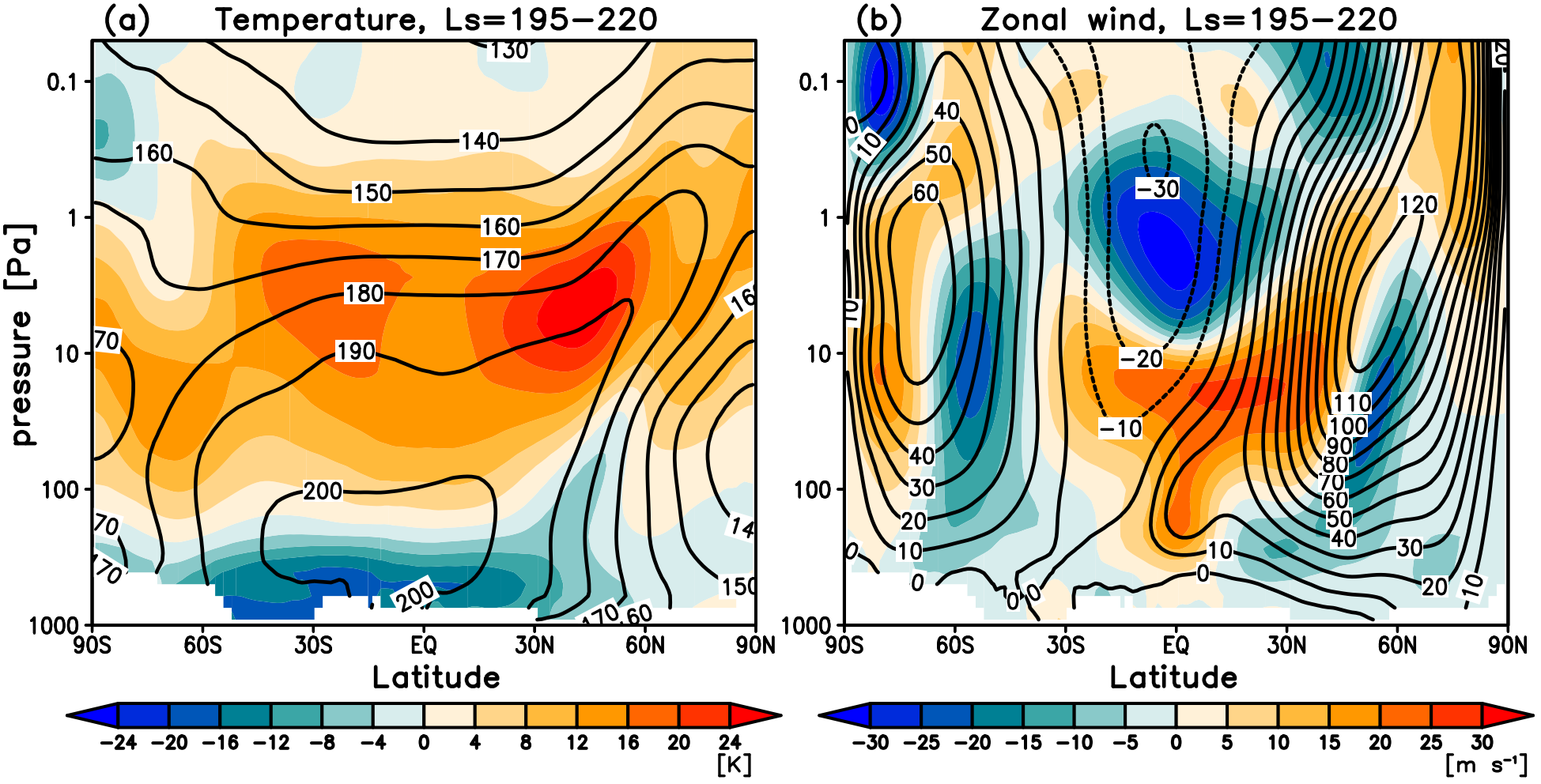
(a) Temperature, Ls=195–220
(b) Zonal wind, Ls=195–220
pressure [Pa]
0.1
1
10
100
1000
90S
60S
30S
EQ
30N
60N
90N
Latitude
−24 −20 −16 −12 −8 −4 0 4 8 12 16 20 24
[K]
−30 −25 −20 −15 −10 −5 0 5 10 15 20 25 30
[m s⁻¹]

Figure 2.

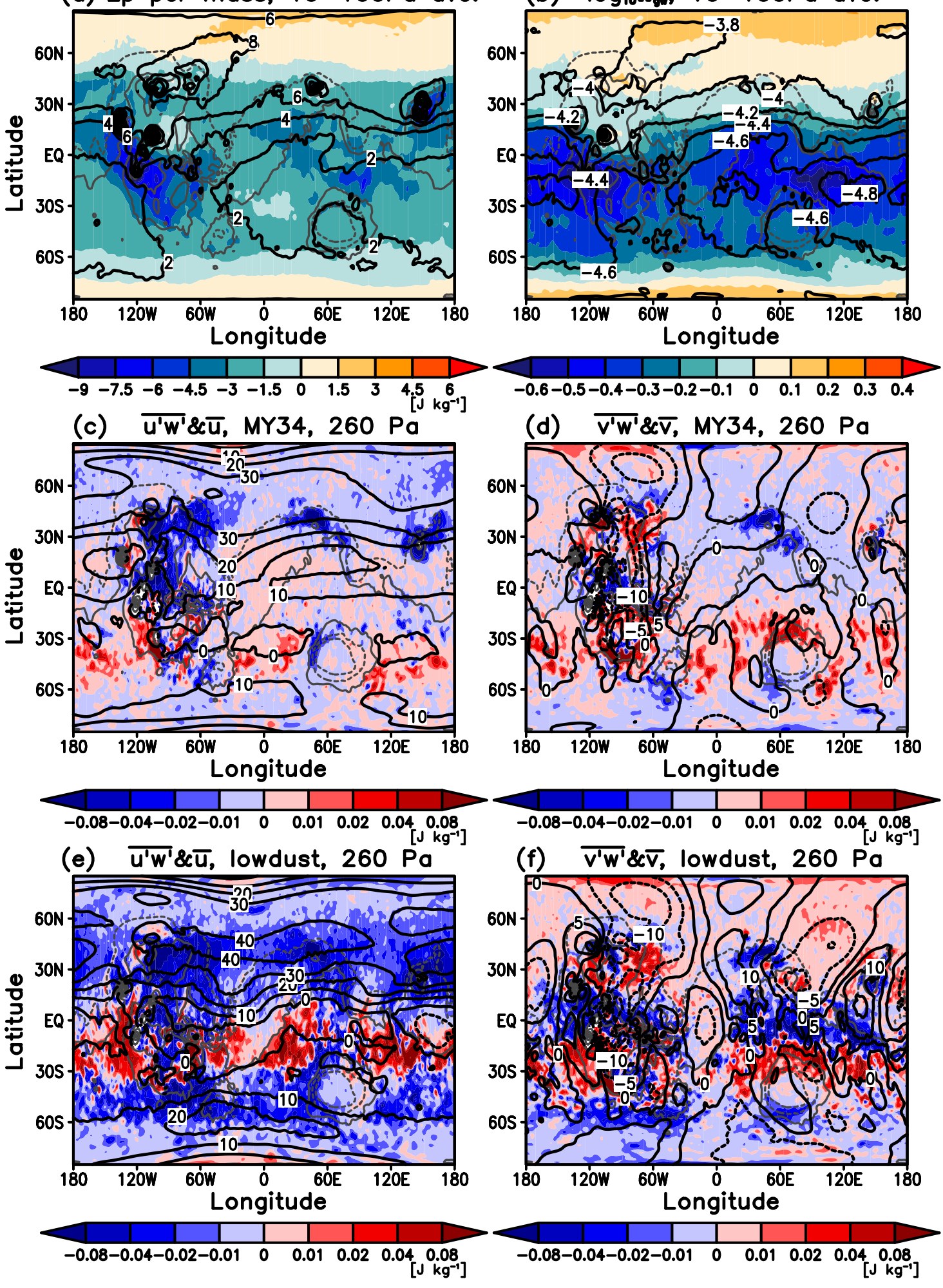
(a) Ep per mass, 10−100Pa ave.
(b) log10Ωgw, 10−100Pa ave.
(c) u'w'&u, MY34, 260 Pa
(d) v'w'&v, MY34, 260 Pa
(e) u'w'&u, lowdust, 260 Pa
(f) v'w'&v, lowdust, 260 Pa
Latitude
Longitude
60N
30N
EQ
30S
60S
180
120W
60W
0
60E
120E
180
−9 −7.5 −6 −4.5 −3 −1.5 0 1.5 3 4.5 6
[J kg⁻¹]
−0.6 −0.5 −0.4 −0.3 −0.2 −0.1 0 0.1 0.2 0.3 0.4
−0.08 −0.04 −0.02 −0.01 0 0.01 0.02 0.04 0.08
[J kg⁻¹]

Figure 3.

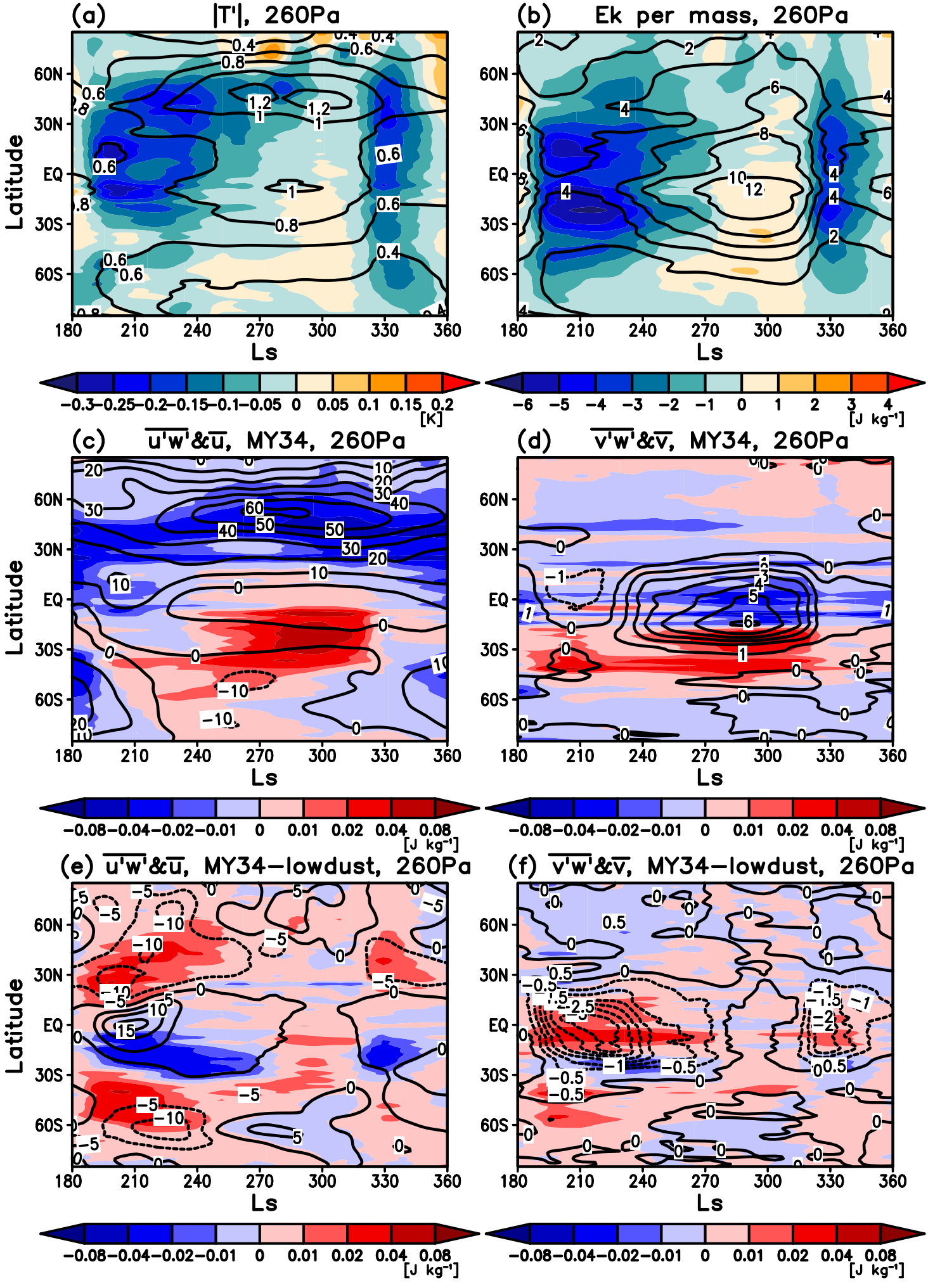
(a) |T'|, 260Pa
(b) Ek per mass, 260Pa
(c) u'w'&u, MY34, 260Pa
(d) v'w'&v, MY34, 260Pa
(e) u'w'&u, MY34−lowdust, 260Pa
(f) v'w'&v, MY34−lowdust, 260Pa
Latitude
60N
30N
EQ
30S
60S
180
210
240
270
300
330
360
Ls
−0.3 −0.25 −0.2 −0.15 −0.1 −0.05 0 0.05 0.1 0.15 0.2
[K]
−6 −5 −4 −3 −2 −1 0 1 2 3 4
[J kg⁻¹]
−0.08 −0.04 −0.02 −0.01 0 0.01 0.02 0.04 0.08
[J kg⁻¹]

Figure 4.

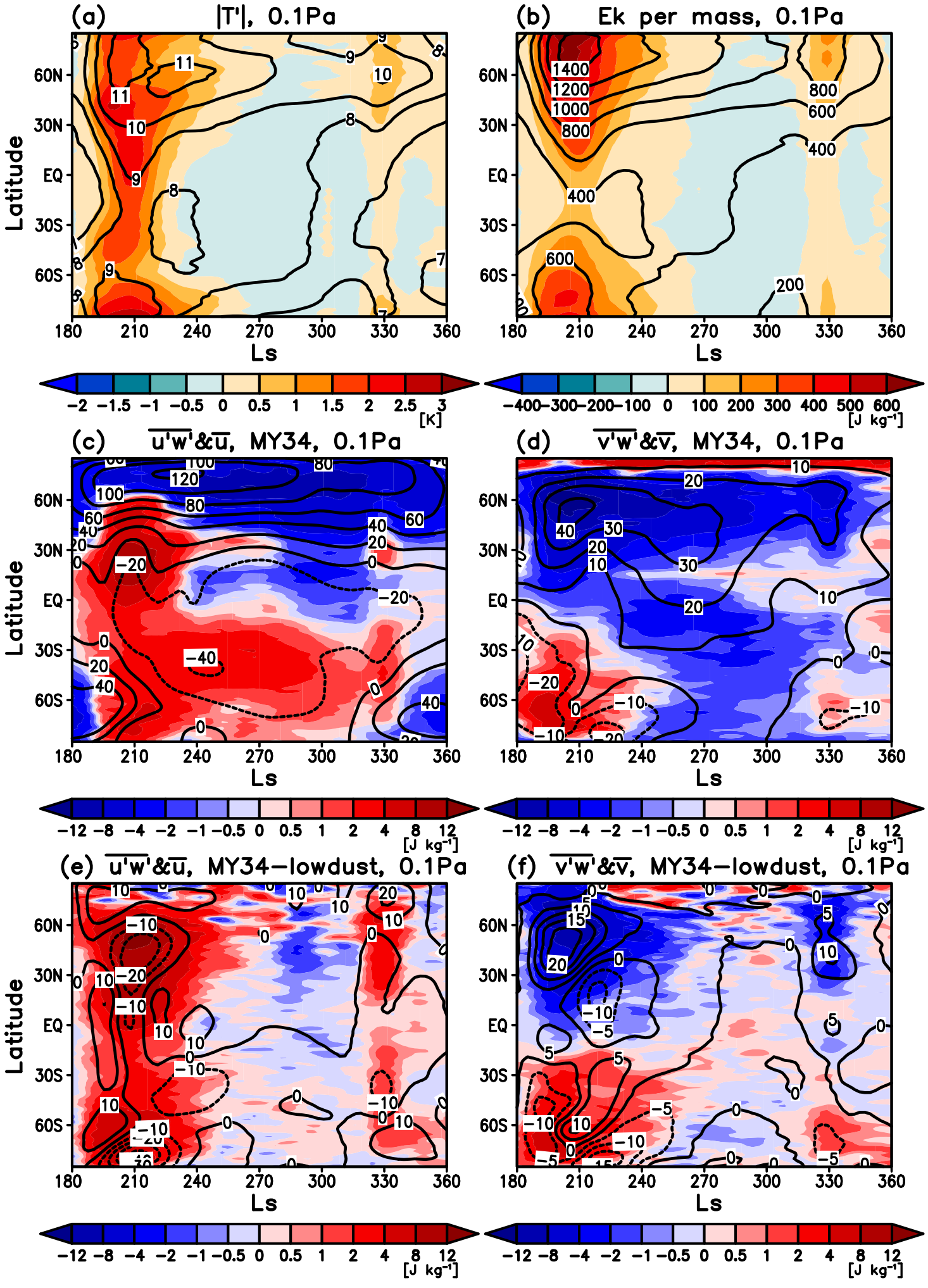
(a) |T'|, 0.1Pa
(b) Ek per mass, 0.1Pa
(c) u'w'&u, MY34, 0.1Pa
(d) v'w'&v, MY34, 0.1Pa
(e) u'w'&u, MY34−lowdust, 0.1Pa
(f) v'w'&v, MY34−lowdust, 0.1Pa
Latitude
60N
30N
EQ
30S
60S
180 210 240 270 300 330 360
Ls
−2 −1.5 −1 −0.5 0 0.5 1 1.5 2 2.5 3
[K]
−400 −300 −200 −100 0 100 200 300 400 500 600
[J kg⁻¹]
−12 −8 −4 −2 −1 −0.5 0 0.5 1 2 4 8 12
[J kg⁻¹]

Figure 5.

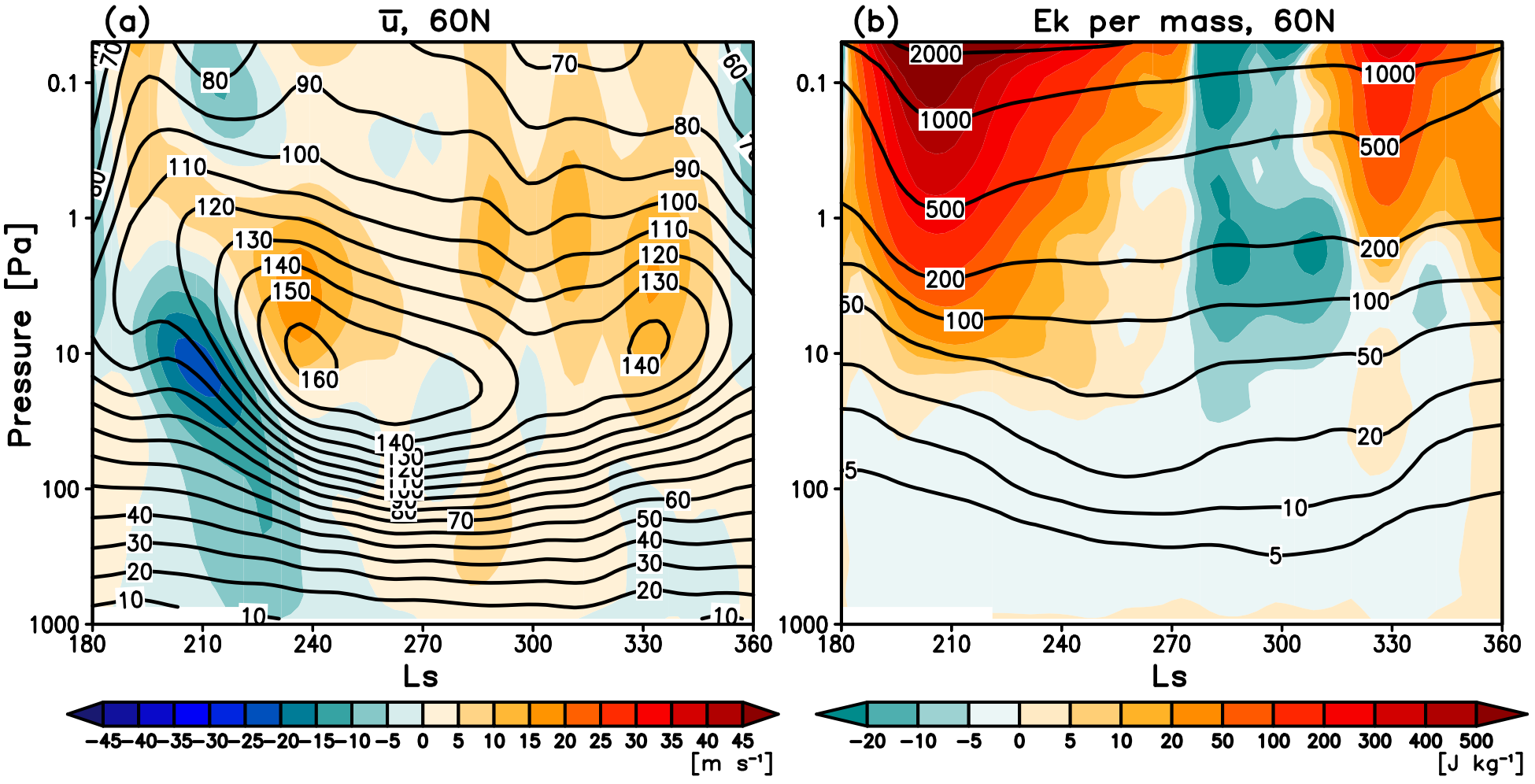
(a)
ū, 60N
(b)
Ek per mass, 60N
Pressure [Pa]
0.1
1
10
100
1000
180
210
240
270
300
330
360
Ls
−45 −40 −35 −30 −25 −20 −15 −10 −5 0 5 10 15 20 25 30 35 40 45
[m s⁻¹]
−20 −10 −5 0 5 10 20 50 100 200 300 400 500
[J kg⁻¹]

Figure 6.

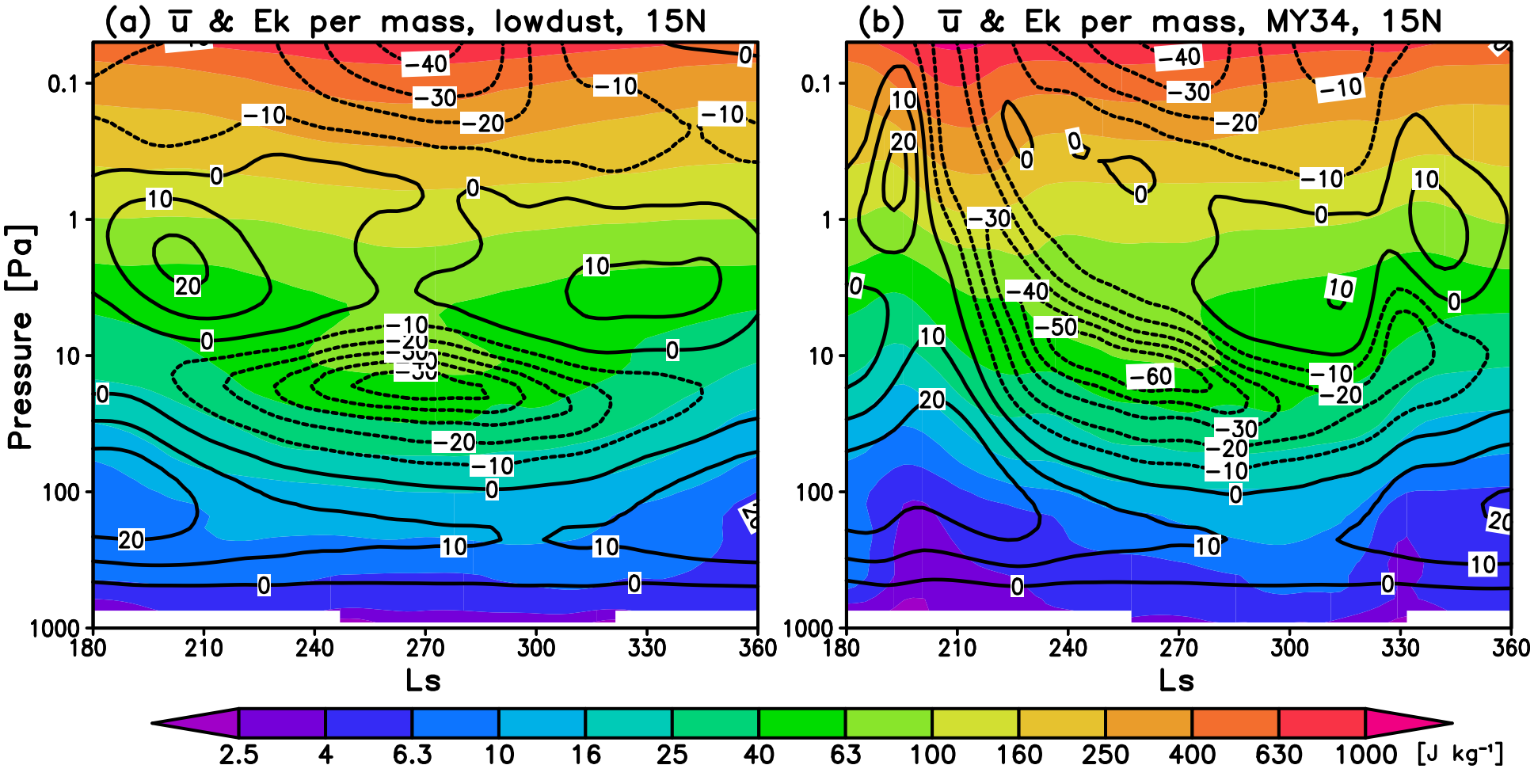
(a) ū & Ek per mass, lowdust, 15N
(b) ū & Ek per mass, MY34, 15N
Pressure [Pa]
0.1
1
10
100
1000
180
210
240
270
300
330
360
Ls
2.5
4
6.3
10
16
25
40
63
100
160
250
400
630
1000
[J kg⁻¹]